JOURNAL OF AIRCRAFT
Vol. 43, No. 1, January–February 2006

Aircraft Acceleration Prediction Due to Atmospheric Disturbances with Flight Data Validation

Billy K. Buck*
AeroTech Research (U.S.A.), Inc., Newport News, Virginia 23606
and
Brett A. Newman†
Old Dominion University, Norfolk, Virginia 23529

A methodology to predict aircraft transient motion resulting from flight within a turbulent atmospheric environment, coupled with validation using flight-test data, is explored. A family of four linear dynamic models is developed for describing the normal acceleration throughout an aircraft cabin due to vertical gust excitation. The four models successively build upon each other by incorporating higher fidelity gust penetration effects while simultaneously maintaining a unified modeling framework. Six wind fields reconstructed from flight-test data are used to excite the vehicle models. Simulation responses are compared with forward, center, and aft accelerometer data streams recorded during the test. Although significant differences are known to exist between the simulated dynamics and flight vehicle, all models tend to approximate adequately primary features in the nonlinear flight data. However, higher-order features in the flight data can not be reliably replicated in the simulations due to these differences. One model consistently tends to out perform the other models, both qualitatively and quantitatively, and corresponds to the highest fidelity gust penetration model. This particular model is recommended as an acceptable alternative to a higher fidelity, nonlinear full simulation when approximating the acceleration response for the intended application.

Nomenclature

a, b = discrete simulation coefficients, s^{-1}
C_{Lx} = coefficient of lift due to variable x, where x is $\alpha, \dot{\alpha}, q$, rad^{-1}
C_{Mx} = coefficient of moment due to variable x, where x is $\alpha, \dot{\alpha}, q$, rad^{-1}
$\bar{c}$ = mean aerodynamic chord, ft
d = load datum, ft
e = normal load error, g
g = acceleration due to gravity, ft/s^2
H = frequency-domain and discrete-domain transfer model, $(g \cdot s)/ft$
h = time step of simulation, s
I_{yy} = aircraft moment of inertia, $slug \cdot ft^2$
K = transfer function gain, $(g \cdot s)/ft$
k_i = discrete simulation coefficient, $i = 1, 2, \ldots, 7$, s except k_4 (nondimensional)
k_y = radius of gyration, ft
L = aerodynamic lag, s^{-1}
M_x = pitch acceleration stability derivative due to variable x, where x is $q, w, \dot{w}$, s^{-1}, $(ft \cdot s)^{-1}$, ft^{-1}
m = aircraft mass, slug
q = pitch rate, body axis, rad/s
q_g = pitch rate gust, body axis, rad/s
S = wing area, ft^2
s = Laplace variable, s^{-1}
t = temporal variable, s
u = longitudinal velocity, body axis, ft/s
W = weight, gross, lbf
w = vertical velocity, body axis, ft/s
w_g = vertical velocity gust, body axis, ft/s
Z_x = vertical acceleration stability derivative due to variable x, where x is $q, w, \dot{w}$, $ft/(rad \cdot s)$, s^{-1}, nondimensional
z = discrete variable, nondimensional
α = angle of attack, rad
β_i = discrete simulation coefficient, $i = 0, 1, 2, 3$, $(g \cdot s)/ft$
γ_i = discrete simulation coefficient, $i = 0, 1, 2$, nondimensional
Δn = normal load, g
η_i = transfer function coefficient, numerator, $i = 1, 2, 3$, s^{-2}, s^{-1}, nondimensional
η_i' = transfer function coefficient, numerator, $i = 2, 3$, s^{-1}, nondimensional
η_i'' = transfer function coefficient, numerator, $i = 2, 3$, s^{-1}, nondimensional
θ = pitch angle, rad
λ_i = transfer function coefficients, denominator, $i = 0, 1$, s^{-2}, s^{-1}
μ = mass parameter, nondimensional
ρ = density of air, $slug/ft^3$

Subscripts and Superscript

cg = center of gravity fuselage station
i = discrete time index
j = model number
rms = root mean square
0 = trimmed variable or flight condition
Δ = change in primary variable
$\cdot$ = time derivative of primary variable

Received 15 July 2004; presented as Paper 2004-4826 at the AIAA Atmospheric Flight Mechanics Conference and Exhibit, Providence, RI, 16–19 August 2004; revision received 14 February 2005; accepted for publication 17 February 2005.

*Aerospace Engineer, 11836 Fishing Point Drive, Suite 200; BillBuck@atr-usa.com. Member AIAA.
†Associate Professor, Department of Aerospace Engineering; newman@aero.odu.edu. Associate Fellow AIAA.

Introduction

THE most economic and practical method to explore innovative concepts and to investigate configuration options at an early stage is to first conduct an analytical and/or simulation study using an appropriate engineering mathematical model of the relevant physics. To go directly to high-fidelity modeling or flight test can cost large sums of money and manpower that may be unavailable,

prohibitive, or expensive. Furthermore, unless one is working for a major commercial airline, airframe manufacturer, or a governmental agency, access to the full envelope, nonlinear, multimillion dollar aircraft simulation database is typically not available.

A work around that has developed over the years has been the creation of less complex and less sophisticated aircraft simulations. A researcher may not require an ability to know how the aircraft reacts in a turn or a climb. Landing or takeoff sequences of flight may also be unnecessary. In general, a researcher may be interested only in an aircraft's response to a selection of particular wind fields (turbulence, vortex, theoretical spectra gust) or command maneuvers (control surface doublet, step, sinusoidal) at a particular trim flight condition. These inquires do not require a large investment in resources to answer the questions of interest. In fact, an approximate simplified dynamic model that exhibits the key features associated with the question of interest, and that de-emphasizes all other aspects, is all that is required by the analyst.[1,2]

One of the simplest forms of an aircraft simulation makes use of a two degree-of-freedom (2-DOF) linear longitudinal model, commonly called the pitch–plunge or short-period model.[3] These models are limited to the assumption that the aircraft forward motion is prescribed with constant speed, longitudinal dynamics are decoupled from the lateral–directional dynamics, and the symmetric motion is a small perturbation about the equilibrium state. This model also typically assumes a gust–vehicle interface that does not account for gust penetration effects on the aircraft (the effect of an aircraft reacting to a gust at the forward and aft stations at different points in time).[4–6] Furthermore, calculation of accelerations throughout the cabin at points other than the mass center is usually not considered. In addition, a 2-DOF model inherently does not incorporate the full control system for the aircraft, but in nearly all cases of modern commercial aircraft, the autopilot or stability augmentation system is operating and influencing the aircraft motion behavior. A controls-fixed simulation, or a researcher-developed control system, may not accurately model an aircraft's closed-loop response to turbulence.

This paper will address development of improved techniques for the prediction of rigid-body aircraft acceleration responses due to atmospheric disturbances.[7,8] In particular, the goal of this paper is to develop and document four different aircraft models and to assess their ability to predict distributed loads across a commercial aircraft's cabin. The four models successively build upon each other, adding increasing degrees of complexity through the inclusion of additional gust excitation terms while at the same time maintaining a standard form for each model to unify implementation in a discrete FORTRAN simulation. The objectives of this paper are to develop an understanding of the improved techniques and validate these techniques using flight-test data. Another objective of the paper is to show the usefulness of an open-loop linear rigid model in predicting the response of an actual nonlinear, flexible, closed-loop aircraft in turbulence.[9] It is hoped that the work developed in this paper will provide additional tools that can be used in aircraft simulation studies.

In the initial step of the investigation, the nonlinear equations of motion (EOM) are developed. Linear air reaction assumptions are applied, and a model family based on nondimensional stability derivatives is developed with an increasing gust penetration fidelity for four individual aircraft models. A generalized framework is developed, which extends for each model an ability to calculate the normal accelerations at points along the aircraft's centerline. With these continuous models and their coefficients, the corresponding discrete models are developed. Each of the models are evaluated using flight-test derived wind field inputs and are compared with three high-frequency accelerometer data streams recorded during the flight test. Final comparative analysis is performed for all of the models at each of the flight conditions for each of the wind fields.

Flight Derived Vertical Wind

The aircraft selected for study in this research work is the Boeing 757-200. Access to flight-test data from a NASA airborne research platform facilitated the selection process. Throughout the cockpit and cabin of the NASA B-757-200, a high-fidelity research system is available to support a variety of flight-test work. Some of the goals in using the transport research system include increasing commercial jet transportation safety and airport/airway system capacity. Under the NASA aviation safety initiative, the Aviation Safety and Security Program was formed. Contained under subelement Weather Accident Prevention program, the Turbulence Prediction and Warning Systems (TPAWS) program was formed. Within these programs, NASA uses the B-757-200 as a flying laboratory to detect, predict, and measure different forms of atmospheric turbulence and its sometimes dangerous effects in an effort to facilitate the development of future aviation safety products,[10] such as cockpit-based real-time load prediction tools using simplified vehicle simulation models.

The Boeing 757-200 is built on advances made in previous aircraft of the Boeing family and has a common design with the Boeing 767 aircraft. The vehicle is a low wing, single-aisle airliner with two turbofan power plants located below the wings. Lifting surface planforms have swept back and tapered characteristics. The flying controls are conventional in nature (not fly-by-wire technology) and are hydraulically powered. With a wing span of 124 ft 10 in., mean aerodynamic chord (mac) of 16 ft 7.7 in., total length of 155 ft 3 in., and a gross wing area of 1,951 ft^2, the B-757-200 is a workhorse of the airline industry. Figure 1 is a schematic of the vehicle and is representative of the NASA B-757.

The vertical wind fields used for comparative analysis in this study are part of a three-dimensional wind vector derived from data taken aboard the NASA B-757-200 research aircraft. The inertial wind vector was derived using high-fidelity aircraft-measured parameters for the NASA TPAWS program.[11] For this work, the vertical wind component of this field is used as the primary input to the simulations. An additional bonus from the aircraft test is the recorded forward, center, and aft accelerometers during the turbulence encounters. Six turbulence encounters by the B757-200 have been selected for the comparison work.

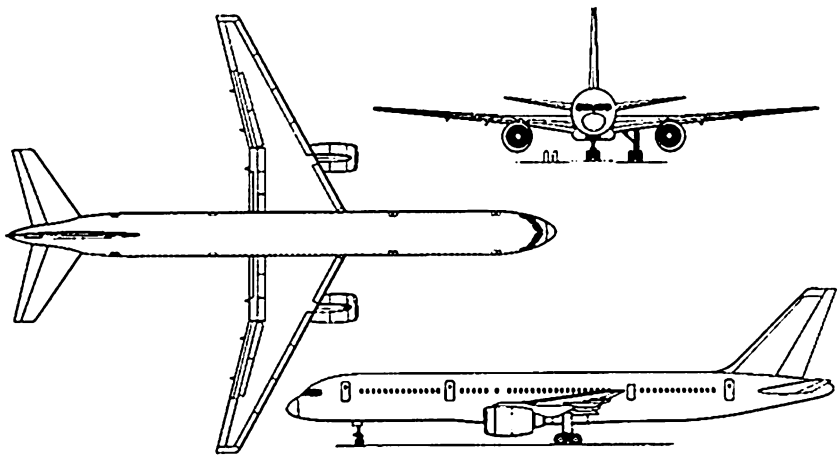

Fig. 1 B-757-200 aircraft layout.

Table 1 Test conditions

Parameter	R191-06	R233-01	R233-04	R235-02	R235-05	R240-09
Turbulence intensity	Severe	Severe	Moderate and low altitude	Moderate	Moderate	Extreme
Altitude, ft	33,000	30,000	15,000	25,000	20,000	25,000
Gross weight, lbf	177,600	190,000	180,000	180,000	170,000	180,000
Gravity center, %mac	19.27	18.00	18.00	18.00	18.00	18.00
Indicated airspeed, kts	279.0	290.0	290.0	290.0	290.0	290.0
True airspeed, ft/s	771.00	761.89	606.60	705.26	653.62	705.26
Angle of attack, deg	2.0200	2.0876	2.187	2.0463	1.9556	2.0463
Pitch angle, deg	2.0200	2.0876	2.187	2.0463	1.9556	2.0463
Pitch inertia, slug · ft^2	4,661,000	4,661,000	4,661,000	4,661,000	4,661,000	4,661,000

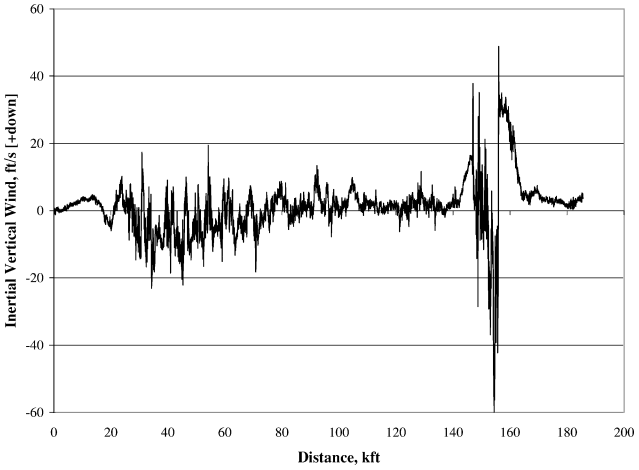

Fig. 2 Vertical wind field, R191-06.

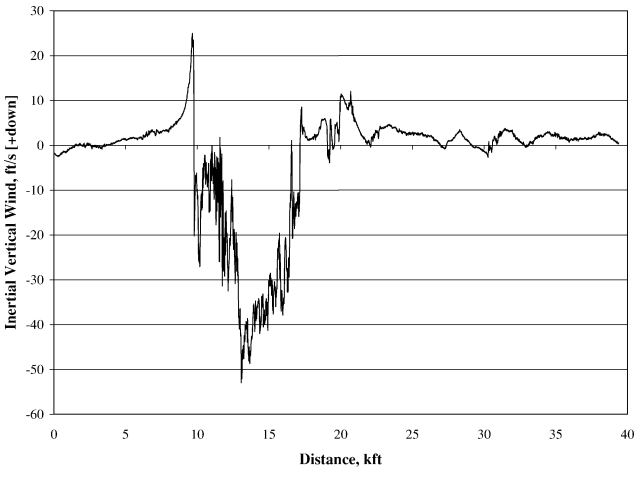

Fig. 3 Vertical wind field, R233-01.

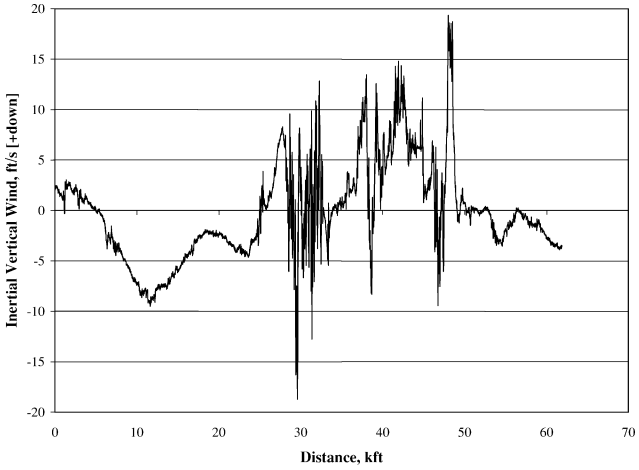

Fig. 4 Vertical wind field, R233-04.

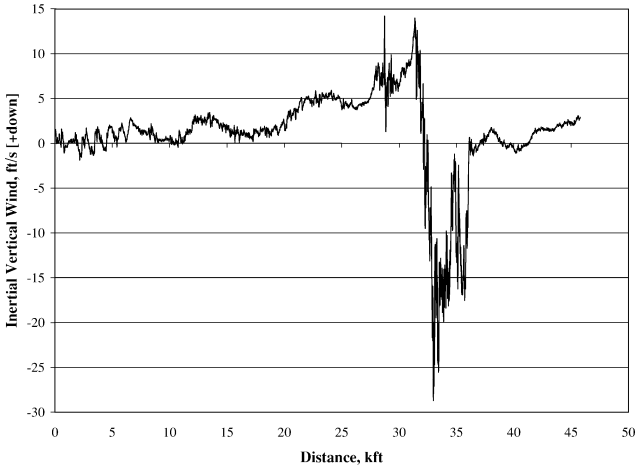

Fig. 5 Vertical wind field, R235-02.

These encounters are moderate to severe in nature and resulted from flights through a convective-induced turbulence environment. Although a commercial airliner would not seek out these hazardous conditions, the turbulence experienced by the B-757-200 can be considered typical. These flight data wind fields provide a significant, real-world test of the models. Comparison analysis will focus on the response of the simulated aircraft to these flight derived vertical wind profiles. Figures 2–7 show the vertical wind used as input to the simulations. Spatial resolution for all six cases is less than 16 ft 5 in., well below the aircraft length of 155 ft. The R###-## descriptor denotes the flight-test recording system. Table 1 lists the trim conditions and turbulence intensities for each of the six encounters. The aircraft equilibrium states for each trim condition are based on average values of the NASA B-757-200 data stream during the turbulence events.

Aircraft Dynamic Models

Using fundamental principles, a general set of nonlinear equations of motion can be derived, from which a linearized set of equations can be extracted.[5] The two primary equations of interest involve the terms $\dot{w}$ and $\dot{q}$. These terms describe the 2-DOF plunge and pitch motion of an aircraft, which provide the largest contribution to vertical acceleration in the aircraft cabin. Several significant assumptions are made in the EOM derivation. The EOM are linearized. The derivation uses the small-angle approximation and assumes the aircraft is a rigid body with a vertical plane of symmetry. The aircraft is in a steady state, wings level, cruise condition with constant mass, and a quasi-static aerodynamic model is assumed. The final assumption is the aircraft model is controls fixed.

Often in an aircraft model simulation development, gust effects of the atmosphere are neglected for various reasons and are removed in the final form of the equations. Here, gust effects are the key excitation of interest. A general set of linear expressions for $\dot{w}$

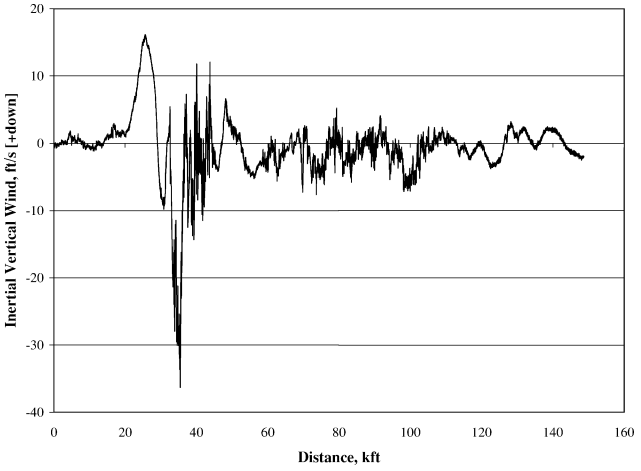

Fig. 6 Vertical wind field, R235-05.

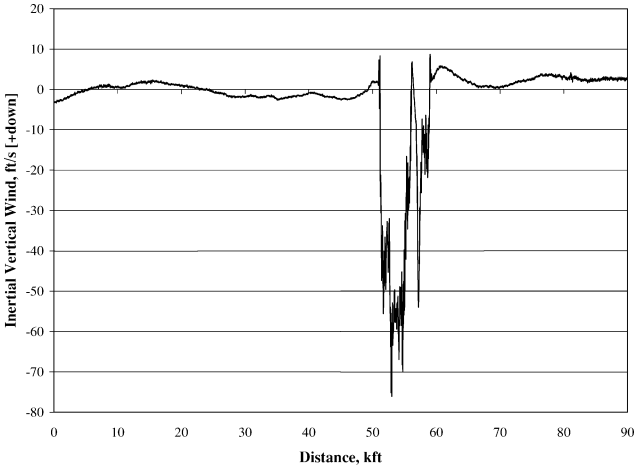

Fig. 7 Vertical wind field, R240-09.

and $\dot{q}$ under the stated assumptions and incorporating gust effects are

$$\dot{w} = Z_w(w - w_g) + Z_{\dot{w}}(\dot{w} - \dot{w}_g) + Z_q(q - q_g) + u_0 q - (g \sin\theta_0)\theta \tag{1}$$

$$\dot{q} = M_w(w - w_g) + M_{\dot{w}}(\dot{w} - \dot{w}_g) + M_q(q - q_g) \tag{2}$$

These equations include vertical gust velocity w_g, positive down, and gust acceleration $\dot{w}_g$ excitations in both plunge and pitch motion and gust pitch rate q_g, positive nose up, excitations as well. The gust pitch rate terms account for gust penetration effects. The Laplace transform is applied to Eqs. (1) and (2) and initial conditions are assumed zero. The final form of the complex frequency-domain expressions are

$$sw(s) = (Z_{\dot{w}}s + Z_w)[w(s) - w_g(s)] + Z_q[q(s) - q_g(s)] + u_0 q(s) - (g \sin\theta_0)\theta(s) \tag{3}$$

$$sq(s) = (M_{\dot{w}}s + M_w)[w(s) - w_g(s)] + M_q[q(s) - q_g(s)] \tag{4}$$

To better understand the gust penetration effect and the mechanism underlying the gust pitch rate term, consider Fig. 8. As the aircraft penetrates a vertical wind gradient, the forward and aft stations experience different winds, which can be interpreted as a rotational gust q_g. This rotational wind can be approximated from the change in position, Δx, and change in vertical gust, Δw_g, occurring during the time interval Δt as indicated in Fig. 8. In the limit, q_g becomes directly proportional to the gust derivative $\dot{w}_g$. Observe that the geometry requires a negative q_g from a positive $\dot{w}_g$. In the complex

Table 2 Model assumptions

Accel. to gust model	Model 1	Model 2	Model 3	Model 4
Pitch Eq. (7)	$\dot{w}_g, q_g = 0$	$\dot{w}_g, q_g \neq 0$	$\dot{w}_g, q_g \neq 0$	$\dot{w}_g, q_g \neq 0$
Plunge Eq. (6)	$\dot{w}_g, q_g = 0$	$\dot{w}_g, q_g = 0$	$\dot{w}_g, q_g \neq 0$	$\dot{w}_g, q_g \neq 0$
Pitch–plunge Eqs. (6) and (7)	$L = 0$	$L = \infty$	$L = \infty$	$0 \leq L \leq \infty$
Plunge Eq. (6)	$\theta_0 = 0$	$\theta_0 = 0$	$\theta_0 = 0$	$\theta_0 = 0$

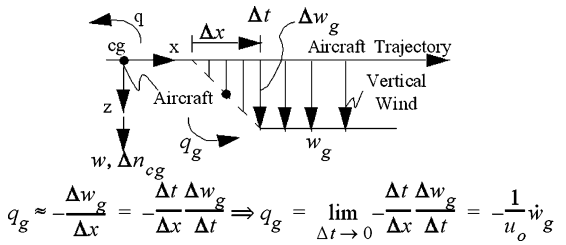

$$q_g \approx -\frac{\Delta w_g}{\Delta x} = -\frac{\Delta t}{\Delta x}\frac{\Delta w_g}{\Delta t} \Rightarrow q_g = \lim_{\Delta t \to 0} -\frac{\Delta t}{\Delta x}\frac{\Delta w_g}{\Delta t} = -\frac{1}{u_o}\dot{w}_g$$

Fig. 8 Gust penetration physics.

frequency domain, the gust penetration term $q_g(s)$ is related to $w_g(s)$ as[4]

$$q_g(s) = -(s/u_0)w_g(s) \tag{5}$$

When the vehicle penetrates an idealized step gust, the wind field gradient is infinite and the signals q_g and $\dot{w}_g$ become impulse excitations under the earlier assumptions of quasi-static aerodynamics and gust penetration physics. Under such a framework, an acceleration from the gust-excited aircraft model will exhibit noncausal or nonproper behavior. The system will respond impulsively to an atmospheric encounter with sharp discontinuities, a theoretical scenario not occurring in practice. Here two independent assumptions have resulted in nonphysical behavior. To correct this gust-modeling inconsistency, a first-order aerodynamic lag will be applied to the derivatives $Z_{\dot{w}}$, Z_q, $M_{\dot{w}}$, and M_q when multiplying signals $\dot{w}_g$ and q_g to restore expected physical behavior. Only lags on $Z_{\dot{w}}$ and Z_q are required to restore the mass center acceleration response, but lags on $M_{\dot{w}}$ and M_q are also necessary to restore off mass center responses. The modified frequency-domain plunge and pitch models are

$$sw(s) = (Z_{\dot{w}}s + Z_w)w(s) - \{Z_{\dot{w}}[L/(s+L)]s + Z_w\}w_g(s) + Z_q q(s) - Z_q[L/(s+L)]q_g(s) + u_0 q(s) - (g \sin\theta_0)\theta(s) \tag{6}$$

$$sq(s) = (M_{\dot{w}}s + M_w)w(s) - \{M_{\dot{w}}[L/(s+L)]s + M_w\}w_g(s) + M_q q(s) - M_q[L/(s+L)]q_g(s) \tag{7}$$

An acceleration to gust model based on Eqs. (6) and (7) will capture the full gust penetration physics without exhibiting impulsive behavior. Note that in reality each aerodynamic derivative should be multiplied by a unique higher-order lag term in a general unsteady aerodynamic theory. Here only the minimal, uniform aerodynamic lag term necessary to restore consistent physical behavior is considered.

Using the preceding equations as a starting point, four models of increasing gust excitation complexity are developed. The assumptions used in each of the models are presented in Table 2. Model 1 is the simplest in form of all of the models. As shown, the $\dot{w}_g$ and q_g gust excitations are zero. Each model beyond model 1 increases in complexity with the relaxation of individual model 1 assumptions. Model 2 considers gust acceleration and gust pitch rate effects in the pitch dynamics, and beyond this, model 3 incorporates these gust excitation signals in the plunge dynamics. Note model 1 is considered a gust point approximation, whereas model 3 accounts for the full-body gust penetration effects. In some sense, model 2 is a sharp transition between these two categories accounting for partial gust penetration physics. The most complex model, model 4, accounts for all gust penetration effects of the aircraft in a meaningful way by incorporating a simple unsteady aerodynamic model with finite lag value L. Model 4 provides a smooth transition between models 1

Table 3 B-757-200 nondimensional stability derivatives

Parameter	R191-06	R233-01	R233-04	R235-02	R235-05	R240-09
$C_{L\alpha}$	6.970	6.775	5.564	6.005	5.757	6.005
$C_{L\dot{\alpha}}$	−7.360	−7.222	−6.291	−6.720	−6.465	−6.720
C_{Lq}	12.06	11.64	9.617	10.52	9.99	10.52
$C_{M\alpha}$	−2.361	−2.260	−2.033	−2.129	−2.068	−2.129
$C_{M\dot{\alpha}}$	−16.23	−15.21	−11.52	−13.21	−12.20	−13.21
C_{Mq}	−37.88	−36.94	−32.65	−34.75	−33.56	−34.75

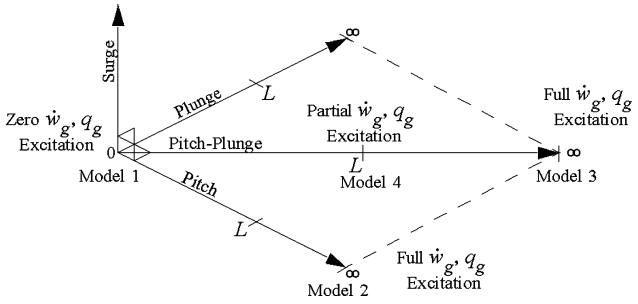

Fig. 9 Model relationships.

and 3. In each model, the gravity component in the plunge dynamics is neglected, $\theta_0 = 0$, because the trim pitch angle is small (Table 1).

Figure 9 is used to further illustrate the various model relationships. Three orthogonal axes describe several models with varying $\dot{w}_g$ and q_g excitation levels parameterized by L in the pitch, plunge, and surge dynamics [Eqs. (7) and (6), and Eq. (3.1–57) in Ref. 7]. Models in this investigation all lie in the pitch–plunge plane; the surge axis is shown only for generalization purposes. Models with zero excitation from $\dot{w}_g$ and q_g (disturbance signal passing through an infinitely slow aerodynamic lag) correspond to the origin, whereas models with full $\dot{w}_g$ and q_g excitation (disturbance signal passing through an infinitely fast aerodynamic lag) correspond to far-off points along each axis. Note that model 1 corresponds to the origin, whereas model 2 corresponds to the far-off point along the pitch axis. Furthermore, model 3 is associated with the far-off point along the simultaneous pitch–plunge direction. Models 2 and 3 both simplify to model 1 as L changes from a value of infinity to zero. This investigation does not consider intermediate models along the pitch axis. However, model 4 is an intermediate model that corresponds to a midpoint along the simultaneous pitch–plunge axis (disturbance signal passing through a finite aerodynamic lag). Observe that model 4 approaches models 1 and 3, respectively, as L approaches zero and infinity. Model 4 actually represents a subfamily of models parameterized by L. Figure 9 is mathematically consistent with Table 2.

For each of the models, a common form of the transfer function for normalized vertical acceleration at the center of gravity, Δn_{cg}, positive down, is developed in a manner that can be implemented in a simulation to produce an estimate of aircraft acceleration due to an input vertical gust. This common form is

$$\frac{\Delta n_{\text{cg}}(s)}{w_g(s)} = K\left[\frac{(s+L)\left(\eta_3 s^3 + \eta_2 s^2 + \eta_1 s\right)}{(s+L)^2\left(s^2 + \lambda_1 s + \lambda_0\right)}\right] \tag{8}$$

To arrive at Eq. (8), the normal load factor is computed from

$$\Delta n_{\text{cg}}(s)/w_g(s) = (1/g)\{s[w(s)/w_g(s)] - u_0[q(s)/w_g(s)]\} \tag{9}$$

The coefficients η_1, η_2, η_3, λ_0, and λ_1 in Eq. (8) have been formed with nondimensional stability derivatives (Table 3) for each of the simulation models and they are as follows, where the notation $\mathcal{O}(1)$ and $\mathcal{O}(L)$ denotes terms of order 1 and L. The nondimensional stability derivatives used for the different models were collected from the NASA B-757-200 simulator trim program under previous contract work. Additional definitions required for the complete description include

$$k_y^2 = \frac{I_{yy}}{m}, \qquad \mu = \frac{2W}{\rho S\bar{c} g C_{L\alpha}} \tag{10}$$

$$K = \frac{\rho S u_0 C_{L\alpha}/(2W)}{1 + (\rho S\bar{c} g/4W)C_{L\dot{\alpha}}} \tag{11}$$

Thus, the model 1 coefficients are

$$\eta_1 = 1\{0\} + \mathcal{O}(L)$$

$$\eta_2 = 1\left\{\frac{1}{2}\left(\frac{1}{2\mu}\right)\left(\frac{\bar{c}}{k_y}\right)^2\left(\frac{2u_0}{\bar{c}}\right) \times \left[\left(\frac{C_{M\alpha}}{C_{L\alpha}}\right)\left(\frac{C_{Lq}+C_{L\dot{\alpha}}}{C_{L\alpha}}\right) - \frac{C_{Mq}+C_{M\dot{\alpha}}}{C_{L\alpha}}\right]\right\} + \mathcal{O}(L)$$

$$\eta_3 = 1\{1\} + \mathcal{O}(L)$$

$$\eta_2'' = 1\{0\} + \mathcal{O}(L)$$

$$\eta_3'' = 1\left\{\left(\frac{1}{2\mu}\right)\left(\frac{\bar{c}}{k_y}\right)^2\left[\frac{C_{M\dot{\alpha}}}{C_{L\alpha}} - \frac{C_{M\alpha}}{C_{L\alpha}}\left(\frac{C_{L\dot{\alpha}}}{C_{L\alpha}} + 2\mu\right)\right]\right\} + \mathcal{O}(L)$$

The model 2 coefficients are

$$\eta_1 = \mathcal{O}(1) + L\left\{\frac{1}{2}\left(\frac{1}{2\mu}\right)\left(\frac{\bar{c}}{k_y}\right)^2\left(\frac{2u_0}{\bar{c}}\right) \times \left[-2\frac{C_{Mq}}{C_{L\alpha}} + \frac{C_{M\alpha}}{C_{L\alpha}}\left(\frac{C_{Lq}+C_{L\dot{\alpha}}}{C_{L\alpha}}\right)\right]\right\}$$

$$\eta_2 = \mathcal{O}(1) + L\left\{1 + \frac{1}{2}\left(\frac{1}{2\mu}\right)\left(\frac{\bar{c}}{k_y}\right)^2 \times \left[\left(\frac{C_{Lq}+C_{L\dot{\alpha}}}{C_{L\alpha}}\right)\left(\frac{C_{M\dot{\alpha}}-C_{Mq}}{C_{L\alpha}}\right)\right]\right\}$$

$$\eta_3 = \mathcal{O}(1) + L\{0\}$$

$$\eta_2'' = \mathcal{O}(1) + L\left\{\left(\frac{1}{2\mu}\right)\left(\frac{\bar{c}}{k_y}\right)^2\left[\frac{C_{Mq}}{C_{L\alpha}} - \frac{C_{M\alpha}}{C_{L\alpha}}\left(\frac{C_{L\dot{\alpha}}}{C_{L\alpha}} + 2\mu\right)\right]\right\}$$

$$\eta_3'' = \mathcal{O}(1) + L\left\{\left(\frac{1}{2\mu}\right)\left(\frac{\bar{c}}{k_y}\right)^2\left(\frac{\bar{c}}{2u_0}\right) \times \left[\left(\frac{C_{Mq}-C_{M\dot{\alpha}}}{C_{L\alpha}}\right)\left(2\mu + \frac{C_{L\dot{\alpha}}}{C_{L\alpha}}\right)\right]\right\}$$

The model 3 coefficients are

$$\eta_1 = \mathcal{O}(1) + L\left\{\left(\frac{1}{2\mu}\right)\left(\frac{\bar{c}}{k_y}\right)^2\left(\frac{2u_0}{\bar{c}}\right)\left[\frac{C_{Lq}C_{M\alpha}}{C_{L\alpha}^2} - \frac{C_{Mq}}{C_{L\alpha}}\right]\right\}$$

$$\eta_2 = \mathcal{O}(1) + L\left\{1 + \left(\frac{1}{2\mu}\right)\left(\frac{\bar{c}}{k_y}\right)^2\left[\frac{C_{Lq}C_{M\dot{\alpha}} - C_{L\dot{\alpha}}C_{Mq}}{C_{L\alpha}^2}\right]\right\}$$

$$\eta_3 = \mathcal{O}(1) + L\left\{\left(\frac{\bar{c}}{2u_0}\right)\left[\frac{C_{L\dot{\alpha}} - C_{Lq}}{C_{L\alpha}}\right]\right\}$$

$$\eta_2'' = \mathcal{O}(1) + L\left\{\left(\frac{1}{2\mu}\right)\left(\frac{\bar{c}}{k_y}\right)^2\left[\frac{C_{Mq}}{C_{L\alpha}} - \frac{C_{M\alpha}}{C_{L\alpha}}\left(\frac{C_{Lq}}{C_{L\alpha}} + 2\mu\right)\right]\right\}$$

$$\eta_3'' = \mathcal{O}(1) + L\left\{\left(\frac{1}{2\mu}\right)\left(\frac{\bar{c}}{k_y}\right)^2\left(\frac{\bar{c}}{2u_0}\right) \times \left[\frac{C_{Mq}}{C_{L\alpha}}\left(\frac{C_{L\dot{\alpha}}}{C_{L\alpha}} + 2\mu\right) - \frac{C_{M\dot{\alpha}}}{C_{L\alpha}}\left(\frac{C_{Lq}}{C_{L\alpha}} + 2\mu\right)\right]\right\}$$

The model 4 coefficients are

$$\eta_1 = 1\{0\} + L\left\{\left(\frac{1}{2\mu}\right)\left(\frac{\bar{c}}{k_y}\right)^2\left(\frac{2u_0}{\bar{c}}\right)\left[\frac{C_{Lq}C_{M\alpha}}{C_{L\alpha}^2} - \frac{C_{Mq}}{C_{L\alpha}}\right]\right\}$$

$$\eta_2 = \frac{1}{2}\left(\frac{1}{2\mu}\right)\left(\frac{\bar{c}}{k_y}\right)^2\left(\frac{2u_0}{\bar{c}}\right)\left[\frac{C_{M\alpha}}{C_{L\alpha}}\left(\frac{C_{Lq}+C_{L\dot{\alpha}}}{C_{L\alpha}}\right) - \frac{C_{Mq}+C_{M\dot{\alpha}}}{C_{L\alpha}}\right] + L\left\{1 + \left(\frac{1}{2\mu}\right)\left(\frac{\bar{c}}{k_y}\right)^2\left[\frac{C_{M\dot{\alpha}}C_{Lq} - C_{L\dot{\alpha}}C_{Mq}}{C_{L\alpha}^2}\right]\right\}$$

$$\eta_3 = 1\{1\} + L\left\{\left(\frac{\bar{c}}{2u_0}\right)\left[\frac{C_{L\dot{\alpha}} - C_{Lq}}{C_{L\alpha}}\right]\right\}$$

$$\eta_2'' = 1\{0\} + L\left\{\left(\frac{1}{2\mu}\right)\left(\frac{\bar{c}}{k_y}\right)^2\left[\frac{C_{Mq}}{C_{L\alpha}} - \frac{C_{M\alpha}}{C_{L\alpha}}\left(\frac{C_{Lq}}{C_{L\alpha}} + 2\mu\right)\right]\right\}$$

$$\eta_3'' = \left(\frac{1}{2\mu}\right)\left(\frac{\bar{c}}{k_y}\right)^2\left[\frac{C_{M\dot{\alpha}}}{C_{L\alpha}} - \frac{C_{M\alpha}}{C_{L\alpha}}\left(\frac{C_{L\dot{\alpha}}}{C_{L\alpha}} + 2\mu\right)\right] + L\left\{\left(\frac{1}{2\mu}\right) \times \left(\frac{\bar{c}}{k_y}\right)^2\left(\frac{\bar{c}}{2u_0}\right)\left[\frac{C_{Mq}}{C_{L\alpha}}\left(\frac{C_{L\dot{\alpha}}}{C_{L\alpha}} + 2\mu\right) - \frac{C_{M\dot{\alpha}}}{C_{L\alpha}}\left(\frac{C_{Lq}}{C_{L\alpha}} + 2\mu\right)\right]\right\}$$

The common coefficients are

$$\lambda_0 = \frac{(2\mu)C_{L\alpha}}{(2\mu)C_{L\alpha} + C_{L\dot{\alpha}}}\frac{1}{2}\left(\frac{1}{2\mu}\right)^2\left(\frac{\bar{c}}{k_y}\right)^2\left(\frac{2u_0}{\bar{c}}\right)^2 \times \left[\frac{C_{M\alpha}C_{Lq}}{C_{L\alpha}^2} - \frac{C_{Mq}}{C_{L\alpha}} - (2\mu)\frac{C_{M\alpha}}{C_{L\alpha}}\right]$$

$$\lambda_1 = \frac{(2\mu)C_{L\alpha}}{(2\mu)C_{L\alpha} + C_{L\dot{\alpha}}}\left(\frac{1}{2\mu}\right)\left(\frac{2u_0}{\bar{c}}\right)\left\{1 - \frac{1}{2}\left(\frac{\bar{c}}{k_y}\right)^2 \times \left[\frac{C_{Mq}+C_{M\dot{\alpha}}}{C_{L\alpha}} + \left(\frac{1}{2\mu}\right)\frac{C_{Mq}C_{L\dot{\alpha}} - C_{M\dot{\alpha}}C_{Lq}}{C_{L\alpha}^2}\right]\right\}$$

The following observations pertain specifically to the center of gravity load factor models. Models 1 and 2 inherently possess a direct feedthrough relationship between vertical gust and normal load (quadratic numerator over a quadratic denominator with zero L for model 1 and infinite L for model 2). For model 3, note a $\mathcal{O}(L)$ nonzero value for η_3 is present. The system transfer function represented here, under the assumptions of a quasi-static aerodynamic model and full gust penetration effects is improper (cubic numerator over a quadratic denominator with infinite L). The system will respond impulsively to an atmospheric encounter with sharp discontinuities, a theoretical nonphysical scenario under the noted assumptions. Model 4 via the aerodynamic lag term restores the direct feedthrough relationship by increasing the system dynamic order (quartic numerator over a quartic denominator with finite L). Note, for model 4, a common factor of $s + L$ can be canceled in the transfer function.

Aircraft Centerline Responses

One of the key comparison points for the simulations is the prediction of normal loads throughout the cabin of a rigid-body aircraft. B-757-200 flight-test data will be used for the comparative analysis, where additional load data for two other accelerometers located in the forward and aft portions of the cabin is provided. A technique must be developed to extend the predicted loads at the simulated center of gravity to another point along the aircraft centerline.

The normalized acceleration at a point along the aircraft's centerline, Δn, under all noted assumptions can be derived and is defined by Eq. (12). The new variable d is the distance to the sensing point along the longitudinal axis of the aircraft relative to the center of gravity. Note that $d > 0$ denotes a location forward of the center of gravity in the simulation model. Thus,

$$\Delta n = \Delta n_{\text{cg}} - (d/g)\dot{q} \tag{12}$$

Equation (12) is rewritten in the s domain to represent accelerations of the rigid body at any point along the centerline of the aircraft as a function of the center of gravity acceleration and pitch rate, resulting from vertical gust excitations. The result is

$$\Delta n(s, d)/w_g(s) = \Delta n_{\text{cg}}(s)/w_g(s) - (d/g)[q(s)/w_g(s)]s \tag{13}$$

The $q(s)$ component in Eq. (13) is rewritten into a compatible form with the earlier defined models as

$$-\frac{d}{g}\frac{q(s)}{w_g(s)}s = K\left(-\frac{d}{\bar{c}}\right)\left[\frac{(s+L)\left(\eta_3''s^3 + \eta_2''s^2\right)}{(s+L)^2\left(s^2 + \lambda_1 s + \lambda_0\right)}\right] \tag{14}$$

Additional coefficients, η_2'' and η_3'', are defined for simplification purposes containing nondimensional stability derivatives. Individual forms of the new coefficients result for the different models. Through a similar method as before, coefficients η_2'' and η_3'' for models 1–4 are as presented earlier.

Equation (14) is now substituted into Eq. (13) and simplified to yield

$$\frac{\Delta n(s, d)}{w_g(s)} = K\left[\frac{(s+L)\left(\eta_3's^3 + \eta_2's^2 + \eta_1 s\right)}{(s+L)^2\left(s^2 + \lambda_1 s + \lambda_0\right)}\right] = H(s, d) \tag{15}$$

where

$$\eta_3' = \eta_3 - (d/\bar{c})\eta_3'', \qquad \eta_2' = \eta_2 - (d/\bar{c})\eta_2'' \tag{16}$$

When the appropriate terms are substituted for coefficients η_1, η_2, η_3, η_2'', η_3'', λ_0, and λ_1, the normal load can be calculated on the aircraft centerline for any of the four simulation models. Note, if $d = 0$, then $\eta_3' = \eta_3$ and $\eta_2' = \eta_2$. Equation (15) now simplifies back to the gravity center form for any of the models. Also note that, for positive $q(s)$ and $\Delta n_{\text{cg}}(s)$, the loads will increase in the rear of the aircraft $d < 0$ and decrease toward the cockpit $d > 0$.

After the sensing point of interest moves off the center of gravity, only model 1 contains a direct feedthrough relationship between vertical gust and normal load (quadratic numerator over a quadratic denominator for zero L). In contrast, models 2 and 3 have an $\mathcal{O}(L)$ nonzero η_3'' coefficient. These systems are nonproper (cubic numerator over a quadratic denominator for infinite L) and will exhibit impulsive behavior when subjected to unsmooth atmospheric disturbances. With the introduction of aerodynamic lag terms, model 4 again restores the direct feedthrough relationship by increasing system dynamic order (quartic numerator over a quartic denominator with finite L). A common factor of $s + L$ again appears in the model 4 transfer function.

Discrete Model Development

The general model Eq. (15) developed in the preceding section and represented by the system diagram in Fig. 10 is a continuous system. For model comparisons with the recorded flight-test data, the simulation should approximate sampled discrete data. A discrete interpretation of the continuous system is developed to cover the variety of aircraft models.

A uniform sample and hold discretization procedure across the model family is desired; however, the commonly used zero-order hold technique is not applicable to nonproper systems.[12] Therefore, to accommodate the nonproper transfer functions, a triangular (also known as trapezoidal) hold[12] sampling procedure was applied to the general continuous system $H(s, d)$ defined earlier in Eq. (15). The new discrete system is shown in Fig. 11. In Fig. 11, h is the time

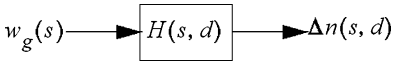

Fig. 10 Continuous aircraft system.

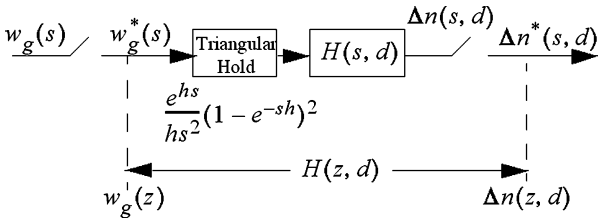

Fig. 11 Expanded discrete aircraft system.

step Δt of the simulation, and the sampling frequency is defined as $1/h$, leading to discrete time $t_i = ih$, where $i = 0, 1, 2 \ldots$. The Z transform[12] ($z = e^{sh}$) is introduced to modify the described system, and the general governing relationship in the z domain is written as

$$\Delta n(z, d)/w_g(z) = (1/h)[(z-1)^2/z]Z\{H(s, d)/s^2\} = H(z, d) \tag{17}$$

After computing the Z transform of $H(s, d)/s^2$, simplifying, and grouping like terms on both sides of the expression,

$$\left(z^3 - \gamma_2 z^2 - \gamma_1 z^1 - \gamma_0 z^0\right)\Delta n(z, d) = \left(\beta_3 z^3 + \beta_2 z^2 + \beta_1 z^1 + \beta_0 z^0\right) w_g(z) \tag{18}$$

Equation (18) is placed into a more usable format for FORTRAN programming by applying the Z transform shifting theorem.[12] This shift is applied to individual normal load and gust variables appearing in Eq. (18). Equation (18) now simplifies down to the following discrete form that can be easily implemented into a digital computer:

$$\Delta n_{i+3} = (\gamma_2 \Delta n_{i+2} + \gamma_1 \Delta n_{i+1} + \gamma_0 \Delta n_i) + \left(\beta_3 w_{g_{i+3}} + \beta_2 w_{g_{i+2}} + \beta_1 w_{g_{i+1}} + \beta_0 w_{g_i}\right) \tag{19}$$

Equation (19) requires the following coefficient definitions:

$$a = \frac{1}{2}\lambda_1, \qquad b = \left(\lambda_0 - \frac{1}{4}\lambda_1^2\right)^{\frac{1}{2}} \tag{20}$$

$$k_1 = \frac{\eta_1}{(a^2 + b^2)L} \tag{21}$$

$$k_2 = \frac{(-1/L)\eta_1 + \eta_2' - L\eta_3'}{(a - L)^2 + b^2} \tag{22}$$

$$k_3 = \frac{(2a - L)\eta_1 - (a^2 + b^2)\eta_2' + L(a^2 + b^2)\eta_3'}{(a^2 + b^2)[(a - L)^2 + b^2]} \tag{23}$$

$$k_4 = \frac{[2a(2a - L) - (a^2 + b^2)]\eta_1 - (2a - L)(a^2 + b^2)\eta_2' + (a^2 + b^2)^2\eta_3'}{(a^2 + b^2)[(a - L)^2 + b^2]} \tag{24}$$

$$k_5 = -k_1(e^{-2ah}e^{-Lh}) - k_2(e^{-2ah}) - k_3[e^{-ah}e^{-Lh}\cos(bh)] + \frac{k_4 - k_3 a}{b}[e^{-ah}e^{-Lh}\sin(bh)] \tag{25}$$

$$k_6 = k_1[2e^{-ah}e^{-Lh}\cos(bh) + e^{-2ah}] + k_2[2e^{-ah}\cos(bh) + e^{-2ah}] + k_3[e^{-Lh} + e^{-ah}(1 + e^{-Lh})\cos(bh)] - \frac{k_4 - k_3 a}{b}[e^{-ah}(1 + e^{-Lh})\sin(bh)] \tag{26}$$

$$k_7 = -k_1[e^{-Lh} + 2e^{-ah}\cos(bh)] - k_2[1 + 2e^{-ah}\cos(bh)] - k_3[1 + e^{-Lh} + e^{-ah}\cos(bh)] + \frac{k_4 - k_3 a}{b}[e^{-ah}\sin(bh)] \tag{27}$$

$$\gamma_0 = e^{-2ah}e^{-Lh}, \qquad \gamma_1 = -2e^{-ah}e^{-Lh}\cos(bh) - e^{-2ah}$$
$$\gamma_2 = e^{-Lh} + 2e^{-ah}\cos(bh) \tag{28}$$

$$\beta_0 = \frac{K}{h}[-k_5], \qquad \beta_1 = \frac{K}{h}[k_5 - k_6]$$
$$\beta_2 = \frac{K}{h}[k_6 - k_7], \qquad \beta_3 = \frac{K}{h}[k_7] \tag{29}$$

Results

Four discrete models for the aircraft acceleration response are excited by six individual wind fields already discussed. For each discrete aircraft model, three fuselage stations (center of gravity at $d \approx 0$ ft, forward station at $d \approx +65.21$ ft, and aft station at $d \approx -52.89$ ft) are considered. The resulting test matrix potentially yields a total combination of 72 individual simulations. In addition to these runs, a step gust is used to characterize fundamental differences in the various aircraft models. Reference 7 contains results for other types of atmospheric disturbances using a slightly different, but related, model family. As a final note, all simulations presented in this section utilize a sample time of $h = 0.02$ s and the wind excitation signals start at $t = 0$ s except for the step gust that starts at $t = 0.06$ s to offset the initial vehicle response from the first two time steps for correct startup verification purposes.

Figure 12 shows the aircraft model responses for normal load at the center fuselage station resulting from a $w_g = +9.84$ ft/s downward step disturbance. The R191-06 flight condition is used in these simulations. Two responses for model 4 are shown in Fig. 12. The model 4 finite aerodynamic lag value is not directly available from the NASA B-757-200 simulator or flight-test data and must be specified. Specified values can be ascertained from approximate minimization of error metrics between simulated and flight-test data, for example, root mean square or maximum peak. Values of $L = 20$ and 200 s^{-1} are used throughout this investigation for model 4 and provide correlation to flight-test data and to the theoretical predicted peak load, where for model 1 this peak value is $K\eta_3 w_g = Kw_g = [(-Z_w/g)/(1 - Z_{\dot{w}})]w_g$. Aerodynamic lag values in the indicated this range are not uncommon in unsteady aerodynamic theories.[13]

For the center station, models 1 and 2 have a direct feedthrough nature and respond instantaneously to the downward step gust at $t = 0.06$ s reaching an acceleration level of $+0.23$ g down and then experience an oscillatory decay back to zero indicative of the short-period frequency and damping. Note the initial response transient is in-phase with the input signal, which is indicative of a gust point approximation. Now consider the initial nonproper model 3 response due to the downward step gust at $t = 0.06$ s. In the continuous domain, model 3 would exhibit an impulse response. Here in the discrete domain, the impulse becomes a finite anticipatory response at $t = 0.04$ s occurring one step before the input signal is applied. This

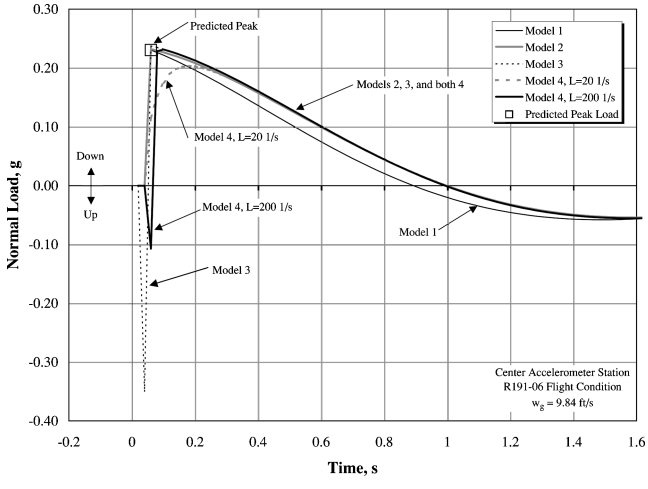

Fig. 12 Model response due to a step gust.

response achieves an acceleration level of -0.35 g upward, then immediately reverses direction to pass near the predicted peak load, followed by oscillatory decay similar to models 1 and 2. The initial response is out-of-phase with the input signal, which is characteristic to full-body gust penetration physics.

Finally, consider the model 4 responses in Fig. 12. This model incorporates all full-body gust penetration terms that are delayed by the aerodynamic pressure buildup lag, which restore the direct feedthrough nature. For $L = 200$ s^{-1}, the response instantaneously reacts to the downward step gust at $t = 0.06$ s and achieves an out-of-phase acceleration transient of -0.10 g upward. A value of $L = 200$ s^{-1} is considered fast, allowing significant pass through of full-body penetration disturbance signals. Observe that the model 4 $L = 200$ s^{-1} response is similar to the model 3 response. For $L = 20$ s^{-1}, the response instantaneously reacts to the downward step gust at $t = 0.06$ s and achieves an in-phase acceleration transient of $+0.12$ g down. A value of $L = 20$ s^{-1} is considered slow, partially attenuating the full-body penetration disturbance signals. Observe that the model 4 $L = 20$ s^{-1} response is more like the model 1 response. Figure 12 exposes the fundamental difference between model 1 and model 3 and shows that model 4 characteristics are an aggregate from models 1 and 3.

To better understand the nonintuitive gust penetration mechanism exhibited in model 3, reconsider Fig. 8 and the initial transmission path from w_g to Δn_{cg} inherent to Eq. (3), (4), and (9). This transmission path can be summarized in Fig. 13. Penetration through a positive step gust w_g leads to a negative impulsive pitch rate gust q_g. This impulse passes through the stability derivative Z_q with sign reversal, yielding a negative upward velocity derivative impulse $\dot{w}$. The $\dot{w}_g$ impulse also passes through stability derivative $Z_{\dot{w}}$ with sign reversal, also yielding a negative upward velocity derivative impulse $\dot{w}$. These signals combine and result in an impulsive normal load transient that is upward and out-of-phase with the original disturbance direction. Therefore, the initial nonintuitive transient associated with the model 3 response depends on the airframe lift due to pitch rate and plunge acceleration characteristics and the rotational and accelerated wind generated over the short duration when the aircraft forward stations have penetrated the step gust while the aft stations have not. Additional transmission paths for off mass center normal load Δn arise from the pitch dynamics in Eqs. (4) and (12). When model 4 is considered, the transmissions indicated in Fig. 13 pass through the aerodynamic lag and compete with other existing in-phase transmission paths, ultimately yielding either a $L = 200$ s^{-1} or $L = 20$ s^{-1} type response. Although the model 3 anticipatory characteristic is theoretical, this analysis suggests initial out-of-phase disturbance responses can occur in practice (model 4, with $L = 200$ s^{-1}). This higher-order gust penetration effect is often ignored even in sophisticated nonlinear flight simulators. Furthermore, measuring such an ultra-short-duration transient may be impractical due to sensor delay and threshold effects.

Figure 14 shows a very small sample of simulated normal load transients for the family of models (model 4 with $L = 200$ s^{-1}) overlaid with the corresponding flight-test recorded acceleration for the R240-09 wind field at the center fuselage station. This sample corresponds to the build up just before the large disturbance near 50,000 ft in Fig. 7. Up to 72 s, data imply the vehicle is in a trimmed flight condition. At 72.2 s, the vehicle reacts to the initial disturbance, reaches a local maximum positive load near 72.3 s, undergoes several smaller transients through the 72.4 s mark, and

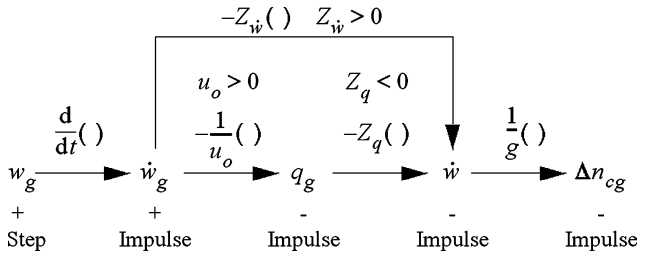

Fig. 13 Disturbance transmission path.

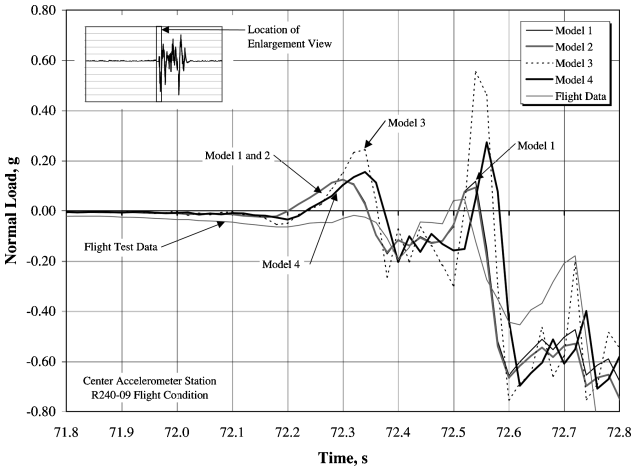

Fig. 14 Acceleration response for R240-09, $L = 200$ s^{-1}.

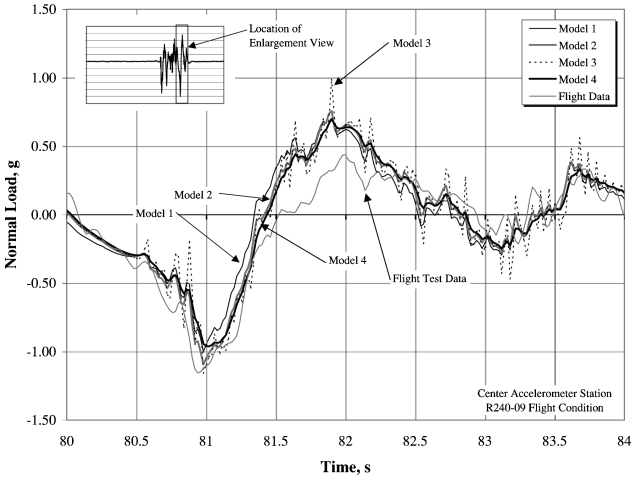

Fig. 15 Center acceleration response for R240-09, $L = 20$ s^{-1}.

then starts another large response at 72.48 s. In this short sequence, note that there are two instances where models 1 and 2 and models 3 and 4 are momentarily out-of-phase, and the response direction of models 3 and 4 correlates with flight data ($t = 72.2$ and 72.48 s). Qualitatively speaking, these two instances have similarities to the step response features shown in Fig. 12. Although not a conclusive argument, observations from Fig. 14 at a minimum suggest the hypothesis that flight data have detected the dynamics of a full-body gust penetration event and that models 3 and 4 have successfully replicated the mechanisms of such an event to first order, whereas models 1 and 2 have not.

Figure 15 shows the normal load response of all aircraft models (model 4 with $L = 20$ s^{-1}) for the R240-09 wind field along with the flight data for the center station. This sample covers a large wind gust event resulting in an amplitude swing of 1.5 g over 1 s and corresponds to 57,000–59,000 ft shown in Fig. 7. All simulated responses consistently group together when responding to the wind field input and tend to track the overall behavior of the recorded data. The most energetic response is from model 3. As expected, this model exhibits high sensitivity to wind fields with sharp gradients resulting in an overprediction of peak values. In contrast, note the attenuating effect from the aerodynamic lag on the model 4 response trace. Although peak load prediction accuracy is sacrificed with respect to models 1–3, the model 4 trace is able to better follow several transients present in the flight data. Qualitative observations lead to the conclusion that model 3 is too sensitive for this type of wind field, and model 4 is at least as good as models 1 and 2 in following the primary flight data transients. Quantitative evaluation also gives a slight edge to model 4. The rms errors $e_{j\text{rms}} = \text{rms}(\Delta n_{\text{cg}_{\text{model}\,j}} - \Delta n_{\text{cg}_{\text{flight}}})$ for each model over the window

in Fig. 15 are $e_{1_{\text{rms}}} = 0.1961\ g$, $e_{2_{\text{rms}}} = 0.1571\ g$, $e_{3_{\text{rms}}} = 0.1939\ g$, and $e_{4_{\text{rms}}} = 0.1513\ g$. For this single evaluation, model 4 is the best closely followed by model 2. Model 3 is less accurate, and model 1 is the least accurate.

In Fig. 15, several higher-order features in the flight-test data can not be reliably replicated by any of the aircraft models. This result is not unexpected. Significant differences are known to exist between the simulated dynamics and the flight vehicle. First, the models are linear approximations and the vehicle is nonlinear. The extreme turbulence in the R240-09 data could easily change the governing aerodynamic coefficients from the trim condition values used by the linear models. Differences noted in Fig. 15 could easily result from this mismatch. Second, the models are rigid-body approximations and the vehicle is flexible. In some sections of the flight data, persistent oscillations in the 20–40 rad/s range are present ($83 \le t \le 83.5$ s shown in Fig. 15). These oscillations could easily originate from structural modes associated with typical commercial transport configurations. The models simply do not contain the appropriate DOF to generate structural vibrations. Furthermore, the unsteady flowfield is significantly more complex than the lag model in Eqs. (6) and (7). Third, the models are open-loop controls fixed and the vehicle is closed-loop controls adjusted. Autopilot control system damping could easily account for the primary overshoot differences noted in Fig. 15 at $t = 82$ s. Pilot maneuvering commands to prevent unsafe upsets or to exit the wind field are also noticeable in other segments of the data streams. Fourth, a less than ideal data acquisition procedure including inconsistent signal sampling and tagging, sensor calibration-bandwidth-delay processing, and unavoidable filtering are realities not incorporated in the models. Other minor sources of mismatch are discussed in Ref. 7. Several of these differences are inaccessible with available data or are unquantifiable under the experimental-test conditions.

Figures 16 and 17 show the forward and aft fuselage station responses corresponding to Fig. 15. All simulated responses again consistently group together when responding to the wind field input and tend to track the gross behavior of the recorded data. The most apparent difference when comparing Figs. 16 and 17 with Fig. 15 is the degraded model 2 responses. Recall that, for off mass center stations, the model 2 η_3'' coefficient is nonzero. Model 2, like model 3 for all stations, becomes overly sensitive to wind fields containing sharp gradients, which is apparent in Figs. 16 and 17. Model 2 overpredicts peak values. On the other hand, model 4 maintains the direct feedthrough nature from the aerodynamic lag, thereby reducing sensitivity to sharp gradients with the tradeoff in peak load prediction accuracy. This mathematical structure, and associated behavior for off center stations, is a key advantage model 4 holds over model 2. From visual inspection, models 2 and 3 are too sensitive for this type of wind field, and furthermore, model 4 is at least as good as model 1 in following the primary flight data transients. As a final observation concerning Figs. 16 and 17, note how the linear models

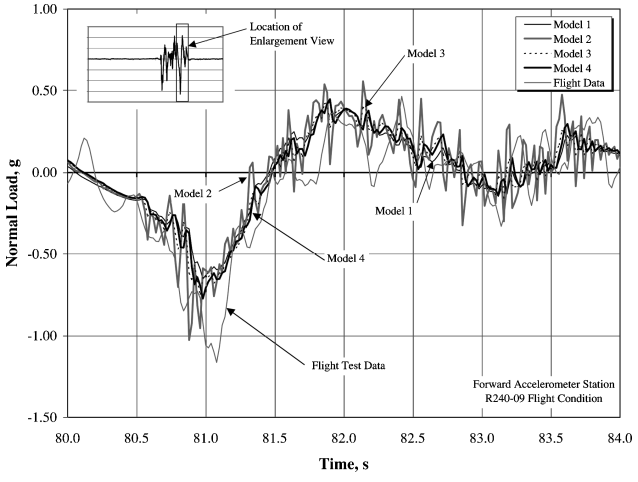

Fig. 16 Forward accelerometer station response for R240-09, $L = 20\ \text{s}^{-1}$.

Table 4 Standard deviation of error difference, $L = 20\ \text{s}^{-1}$

Fuselage station	$\sigma(\Delta n_{\text{model}} - \Delta n_{\text{flight data}})$, g			
	Model 1	Model 2	Model 3	Model 4
		R191-06		
Forward	0.1191	0.1625	0.1184	0.1187
Center	0.0994	0.0997	0.1421	0.0877
Aft	0.1670	0.2043	0.2567	0.1509
		R233-04		
Forward	0.1492	0.2263	0.1566	0.1527
Center	0.1186	0.1102	0.1671	0.0973
Aft	0.1967	0.2588	0.3439	0.1620
		R235-05		
Forward	0.0381	0.0564	0.0402	0.0388
Center	0.0310	0.0295	0.0440	0.0273
Aft	0.0455	0.0564	0.0756	0.0377
		R240-09		
Forward	0.1734	0.2075	0.1620	0.1583
Center	0.1961	0.1571	0.1939	0.1513
Aft	0.2867	0.2681	0.3193	0.2171

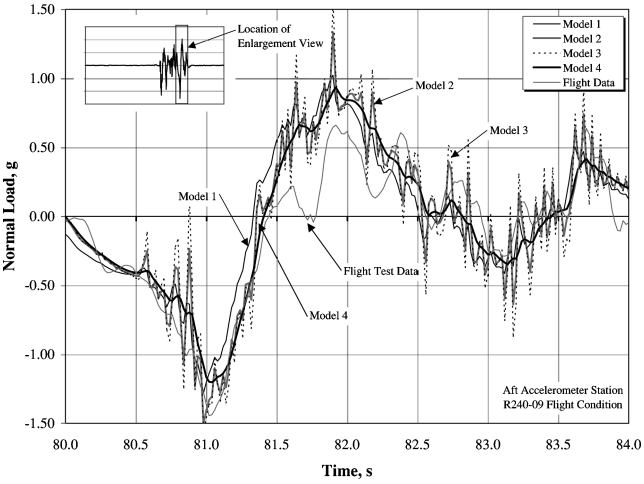

Fig. 17 Aft accelerometer station response for R240-09, $L = 20\ \text{s}^{-1}$.

properly reflect the enhanced loading at the aft station and corresponding reduction at the forward station ($t = 81$ and $t = 82$ s), as well an inability to replicate the 12 rad/s oscillation likely originating from structural dynamics. Other traces are available for the remaining wind fields but are not provided. Trends in Figs. 15–17 are representative of the entire data set.

Table 4 presents overall comparison results from four of the test wind field conditions for the standard deviation of the error difference of a particular model within the family: $e_{j_{\text{rms}}} = \text{rms}(\Delta n_{\text{cg}_{\text{model}\,j}} - \Delta n_{\text{cg}_{\text{flight}}})$. Presented values were determined from portions of the wind fields where a consistent match was available between the resulting model data and the flight data. The two eliminated wind field conditions are from R233-01 and R235-02 turbulence encounters. For these two encounters, the match between the simulation data and flight data presented inconsistencies that are attributed to the nonlinearity in the turbulence encounter and possible inputs from the automatic control system and pilot. Data accuracy of the B-757-200 during these two encounters is also uncertain. The time segment selected for results presented in Table 4 for R191-06 is 43–47 s, for R233-04 is 46–54 s, for R235-05 is 106–125 s, and for R240-09 is 80–84 s. The aerodynamic lag L used for model 4 in Table 4 is $20\ \text{s}^{-1}$. In general, inspection of the values presented shows that model 4 tends to have the lowest values within the family of models for the center and aft accelerometer stations. When the forward accelerometer station is considered, model 4 is only out ranked by model 1 in two of the four wind fields, and then only by a small difference. The overall trend for standard deviation of the error difference for the family of models from better to worse is model 4, then model 2, followed by model 1 and then model 3.

Model 3 is generally the worst match in the family of four when considering the center and aft accelerometer stations, and model 2 is generally the worst match in the family when considering the forward fuselage station. Examples of these conclusions can be seen in Figs. 15–17. It can be concluded from the results presented within Table 4 that model 4 provides a better approximation of the flight data for each turbulence encounter than the other family members on the whole.

Conclusions

Methodology to predict aircraft transient motion resulting from flight within a turbulent atmospheric environment, coupled with validation using flight-test data, has been investigated across a family of four vehicle models with varying degrees of gust penetration fidelity. Derivations showed mathematical model predicted acceleration behavior is nonphysical for wind fields containing sharp gradients when the independent assumptions of quasi-static aerodynamics and full-body gust penetration excitations are applied simultaneously (model 3 nonphysical $\Delta n_{\text{cg}} - \Delta n$ for $\dot{w}_g - q_g$ in pitch–plunge dynamics, model 2 nonphysical Δn for $\dot{w}_g - q_g$ in pitch dynamics). This deficiency was overcome by inclusion of aerodynamic lags on the full-body gust penetration disturbances (model 4). Invariance to sensing location and the presence of sharp wind field gradients is a key advantage model 4 holds over models 2 and 3. Although model 1 achieves similar invariance by elimination of specific disturbance signals, model 4 achieves invariance with these same signals and their associated mechanisms in place. All four linear open-loop models are capable of predicting, with flight-test data validation, the primary motions of the nonlinear closed-loop vehicle resulting from moderate to severe disturbances. Because of known differences, none of the models is capable of reproducing many higher-order features present in the flight data. However, in the application of real-time cockpit-based load prediction using weather radar data and simplified vehicle simulation models, this type of error is acceptable. Qualitative and quantitative assessment of simulated responses benchmarked against the flight-test data suggest model 4 is a leading candidate for such applications.

Acknowledgments

Data used in the presented research were collected by AeroTech Research (U.S.A.), Inc., under the NASA Aviation Safety and Security Program, Weather Accident Prevention Program Element, Contract BPA E-03220D. Appreciation and thanks are extended to Roland Bowles of AeroTech Research (U.S.A.), Inc., for his technical guidance. Additional appreciation is extended to Gustav Taylor for providing NASA B-757-200 simulator response data.

References

[1]Mitchell, D. G., and Hoh, R. H., "Low-Order Approaches to High-Order Systems: Problems and Promises," *Journal of Guidance, Control and Dynamics*, Vol. 5, No. 5, 1982, pp. 482–489.

[2]Newman, B. A., and Schmidt, D. K., "Numerical and Literal Aeroelastic Vehicle Model Reduction for Feedback Control," *Journal of Guidance, Control and Dynamics*, Vol. 14, No. 5, 1991, pp. 943–953.

[3]McRuer, D., Ashkenas, I., and Graham, D., *Aircraft Dynamics and Automatic Control*, Princeton Univ. Press, Princeton, NJ, 1973, Chap. 5, pp. 307, 308.

[4]Houbolt, J. C., "Atmospheric Turbulence," *AIAA Journal*, Vol. 11, No. 4, 1973, pp. 421–437.

[5]Etkin, B., *Dynamics of Atmospheric Flight*, Wiley, New York, 1972, Chap. 13, pp. 544–548.

[6]Etkin, B., "The Turbulent Wind and Its Effect on Flight," *Journal of Aircraft*, Vol. 18, No. 5, 1981, pp. 327–345.

[7]Buck, B. K., "Prediction of Rigid Body Aircraft Acceleration Response Due to Atmospheric Disturbances," M.S. Thesis, Dept. of Aerospace Engineering, Old Dominion Univ., Norfolk, VA, May 2004.

[8]Buck, B. K., Bowles, R. L., and Newman, B. A., "Aircraft Acceleration Prediction Due to Atmospheric Disturbances with Flight Data Validation," AIAA Paper 2004-4826, Aug. 2004.

[9]Prince, J. B., and Robinson, P. A., "The Effectiveness of Linear Aircraft Simulations in Predicting Cabin Loads Induced by Turbulence," AIAA Paper 2001-4139, Aug. 2001.

[10]Green, W. S., Tsoucalas, G., and Tanger, T., "Concept of Operations for the NASA Weather Accident Prevention (WxAP) Project, Version 2.0," NASA TM-2003-212424, NASA Langley Research Center, Hampton, VA, Sept. 2003.

[11]Buck, B. K., Prince, J. B., and Robinson, P. A., "In Situ Algorithm Development and Implementation on the NASA B-757 Simulator and Aircraft, Version 4.0," AeroTech Research (U.S.A.), Inc., ATR-12022, Hampton, VA, Oct. 2001.

[12]Smith, J. M., *Mathematical Modeling and Digital Simulation for Engineers and Scientists*, 2nd ed., Wiley-Interscience, New York, 1987, Chap. 2, pp. 120–125, 141, 142.

[13]Heeg, J., and Dowell, E. H., "Aerodynamic and Aeroelastic Insights Using Eigenanalysis," AIAA Paper 99-1473, April 1999.